AI-Driven Wind Risk Prediction: A Framework for Translating Weather Forecasts to Real-Time Power Grid Resilience

You Wu
College of Civil Engineering and Architecture
Zhejiang University
Hangzhou, China
youwu@zju.edu.cn

Zhenguo Wang
State Grid Zhejiang Electric Power Co., Ltd., Electric Power Science Research Institute
Hangzhou, China
wangzhenguo12@outlook.com

Naiyu Wang
College of Civil Engineering and Architecture
Zhejiang University
Hangzhou, China
naiyuwang@zju.edu.cn

***Abstract*—New-generation AI weather prediction (AIWP) models like Pangu-Weather can generate global forecasts in seconds, but their coarse (e.g., 25-km) resolution and inherent biases make them unusable for direct power grid risk assessment. This paper presents an AI-driven framework that bridges this "implementation gap" by translating raw AIWP forecasts into real-time, asset-level failure probabilities for power transmission grids. The framework first corrects storm-scale biases using a spatiotemporal graph neural network and then downscales the field to 500-m resolution using a terrain-aware transformer-based model. These high-fidelity hazard fields then drive a fragility-based risk model to forecast tower and line failure probabilities. Tested on Typhoon Hagupit (2020), the framework successfully predicted the failure of a real-world transmission line with a 5-h lead time, whereas the raw Pangu forecast showed zero risk. This work provides a validated, end-to-end pathway from global AI forecasts to actionable risk prediction.**

***Index Terms*—Power system resilience, risk analysis, tropical cyclone, weather forecasting**

I. Introduction

Tropical cyclones (TCs) are among the most damaging natural hazards, repeatedly disrupting critical infrastructure, especially power transmission systems [1-3]. Accurate, asset-level failure forecasts are central to proactive resilience: they allow operators to pre-position repair crews, de-energize vulnerable spans, and adjust network topology to reduce cascading risk. Historically, such risk forecasts have relied on physics-based Numerical Weather Prediction (NWP) models (e.g., Weather Research and Forecasting (WRF) model). Although NWP can deliver detailed fields, the required computational resources and multi-hour runtimes on supercomputers limit their usefulness for real-time decision-making during rapidly evolving storm conditions.

Recent AI Weather Prediction (AIWP) models such as Pangu-Weather [4] and GraphCast [5] offer a step-change in speed, delivering global forecasts in minutes. Many AIWP systems also support rapid ensemble generation, which enables multi-scenario hazard simulation and risk anticipation. With compact ensembles, operators can interrogate the most-likely trajectory and intensity while stress-testing plausible worst-case outcomes, thereby obtaining actionable risk bands for timely decisions. However, speed and ensemble size do not by themselves close the fidelity gap for grid operations: AIWP outputs remain relatively coarse (tens of kilometers), may inherit biases from reanalysis-based training data, and do not resolve sub-kilometer terrain effects (e.g., ridge speed-up and valley channeling) that control loads on individual towers [6]–[8]. Using raw AIWP fields for risk assessment can therefore be dangerously unconservative. Existing refinement approaches often treat bias correction and downscaling in isolation: correction reduces systematic errors but cannot introduce terrain-driven details [8], [9], whereas downscaling adds spatial structure but may amplify inherited forecast biases [6], [10]. This disconnect motivates a coupled framework that produces wind fields that are both bias-reduced and geographically realistic for reliable risk assessment.

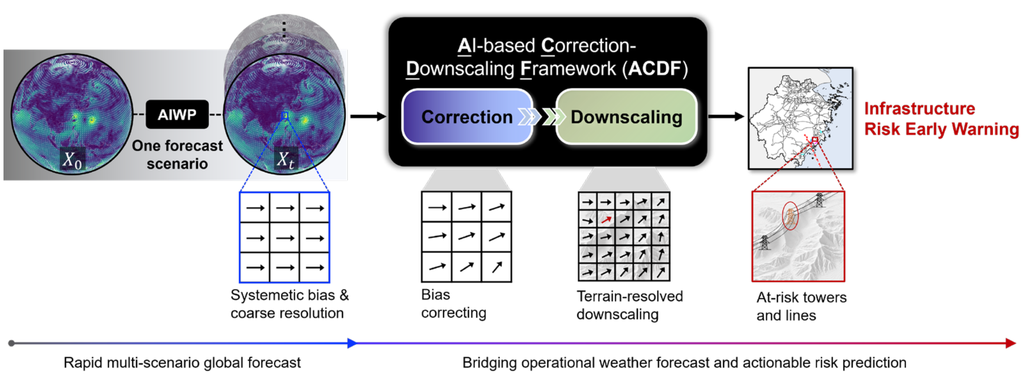

Figure 1. Conceptual overview of the proposed AI-based Correction–Downscaling Framework (ACDF).

979-8-3315-8138-1

To bridge this implementation gap, we introduce the AI-based Correction–Downscaling Framework (ACDF), which translates coarse, biased AIWP forecasts into actionable risk predictions. ACDF ingests raw AIWP outputs to (i) correct storm-scale biases and (ii) downscale winds to engineering resolution with explicit terrain effects (Fig. 1). The resulting high-fidelity hazard fields are coupled with component fragility models to deliver real-time failure probability forecasts for individual transmission towers and lines. ACDF is ensemble-ready: when driven by AIWP ensembles, it yields multi-scenario risk maps from the most-likely to adverse cases, supporting robust, operations-focused decision-making. The main contributions of this work are:

- **An AIWP-Driven Framework:** We present, to our knowledge, the first complete workflow that translates advanced AIWP forecasts (e.g., Pangu-Weather) into operational, asset-level risk predictions for power systems.
- **Decoupled Correction-Downscaling Strategy:** We develop a two-stage deep learning-based architecture that separates storm-scale bias correction (Stage 1) from terrain-aware downscaling (Stage 2), thereby improving meteorological accuracy while delivering 500-m engineering-scale resolution.
- **Validated Risk Forecasting Pipeline:** Using a real-world case study of Typhoon Hagupit (2020), we show that ACDF predicts the failure of a specific transmission line with a 5-h lead time, an event entirely missed by the raw AIWP forecast.

II. Problem Formulation

The core challenge is to translate a coarse, biased, and terrain-agnostic AIWP forecast into a high-resolution, unbiased, and terrain-aware failure probability map for a specific power grid. This requires bridging two distinct gaps: the "Hazard Gap" and the "Risk Gap."

A. The Hazard Gap

The Hazard Gap is the discrepancy between the AIWP output and the true, asset-scale wind hazard. An AIWP wind forecast, $\boldsymbol{X}_{\text{pangu}} \in \mathbb{R}^{(H+\tau)\times N\times 2}$, provides wind vectors for N coarse grid points over H historical and τ future hours. The desired output is a high-resolution hazard forecast, $\widehat{\boldsymbol{Y}}_{\text{ds}} \in \mathbb{R}^{\tau\times H'\times W'\times 2}$, over a fine-resolution grid ($H' \times W'$). This translation must be conditioned on historical coarse-resolution observation, $\boldsymbol{X}_{\text{LR-obs}} \in \mathbb{R}^{H\times N\times 2}$, and high-resolution static terrain data, $\boldsymbol{X}_{\text{terrain}}$.

This requires a mapping $\mathcal{F}$:

$$\widehat{\boldsymbol{Y}}_{\text{ds}} = \mathcal{F}(\boldsymbol{X}_{\text{pangu}}, \boldsymbol{X}_{\text{LR-obs}}, \boldsymbol{X}_{\text{terrain}}) \tag{1}$$

We decompose this mapping into two stages:

1. Correction ($\mathcal{F}_1$): Adjusts storm-scale intensity and track biases to obtain a corrected coarse-field forecast.

$$\widehat{\boldsymbol{X}}_{\text{corr}} = \mathcal{F}_1(\boldsymbol{X}_{\text{pangu}}, \boldsymbol{X}_{\text{LR-obs}}) \tag{2}$$

2. Downscaling ($\mathcal{F}_2$): Converts the corrected forecast $\widehat{\boldsymbol{X}}_{\text{corr}}$ into a terrain-conditioned 500 m wind field $\widehat{\boldsymbol{Y}}_{\text{ds}}$.

$$\widehat{\boldsymbol{Y}}_{\text{ds}} = \mathcal{F}_2(\widehat{\boldsymbol{X}}_{\text{corr}}, \boldsymbol{X}_{\text{terrain}}) \tag{3}$$

B. The Risk Gap

The Risk Gap is the discrepancy between the physical wind hazard field ($\widehat{\boldsymbol{Y}}_{\text{ds}}$) and the operational decision variable: asset failure probability. We therefore seek a mapping that combines the time-varying wind hazard with grid vulnerability information (tower fragility) to compute failure probabilities. Specifically, the mapping converts wind speed $v_j(t)$ (and attack angle) at each tower j into a cumulative line failure probability $P_{line,i}$ for each transmission line i.

III. Methodology

Our methodology is a sequential pipeline: (1) acquire multi-source datasets, (2) process the AIWP forecast through the ACDF to bridge the Hazard Gap, and (3) feed the resulting high-resolution wind fields into a fragility model to bridge the Risk Gap.

A. Dataset

The framework is trained and validated on a comprehensive dataset covering 11 TCs in Zhejiang, China (i.e., 1211 Haikui, 1810 Ampil, 1812 Jongdari, 1814 Yagi, 1818 Rumbia, 1909 Lekima, 1918 Mitag, 2004 Hagupit, 2106 In-fa, 2114 Chanthu, and 2212 Muifa). The dataset includes: (1) AIWP forecasts (Pangu-Weather is used for illustration); (2) gridded analyses (HRCLDAS [11]) and 2,513 station observations for bias correction; (3) WRF simulations (500-m resolution) to provide high-resolution labels for downscaling pre-training; and (4) static data, including a 500-m DEM and the 220/550-kV transmission grid topology (32,458 towers) in Zhejiang Province, China.

B. AIWP-driven ACDF Framework

The ACDF framework (Fig. 1) is a two-stage deep learning model designed to execute the mappings $\mathcal{F}_1$ and $\mathcal{F}_2$.

Stage 1: Correction ($\boldsymbol{\mathcal{F}_1}$). A spatiotemporal graph neural network [12] is employed to model the error evolution between forecasts and observations. It operates on a sliding window, ingesting the past 6 hours of observations and the full 18-hour (6-h past & 12-h future) Pangu forecast, to stay synchronized with common 6-h operational cycling and incorporate the most recent observational increment for real-time correction. Internally, the module uses interleaved Temporal Convolution blocks with gated dilated inception layers to capture time-varying error patterns, and Graph Convolution blocks with mix-hop propagation to model spatial error dependencies across the grid. The network predicts a correction field $\Delta\boldsymbol{X}_{corr}$ which is added to the raw AIWP output via a residual connection:

$$\widehat{\boldsymbol{X}}_{\text{corr}} = \boldsymbol{X}_{\text{pangu}} + \Delta\boldsymbol{X}_{corr} \tag{4}$$

This design effectively removes systematic biases such as intensity underestimation and track shifts.

Stage 2: Downscaling ($\boldsymbol{\mathcal{F}_2}$). To bridge the gap between this bias-corrected background flow and local variability, the downscaling module utilizes a U-Net architecture with Transformer blocks [13]. By using the physically consistent coarse field from Stage 1 as a foundation, this stage injects terrain-driven details. It begins by concatenating the bilinearly interpolated coarse wind field with 500-m static terrain features (e.g., elevation and land use). The hierarchical encoder-decoder structure extracts multi-scale interactions between the airflow and topography, while skip connections preserve high-

979-8-3315-8138-1

frequency spatial details. The model is trained to predict the residual difference between the coarse input and the high-fidelity ground truth, effectively superimposing local terrain-driven effects such as ridge speed-ups and valley channeling onto the background flow to produce the final 500-m hazard forecast $\widehat{\boldsymbol{Y}}_{\mathrm{ds}}$. This resolution is determined by the high-fidelity WRF training labels, representing a scale that effectively captures the topographic accelerations governing transmission line loading in complex terrain. Importantly, the downscaling module is trained with a dual-supervision loss function:

$$\mathcal{L}_{total} = \mathcal{L}_{grid} + \alpha \mathcal{L}_{station} \tag{5}$$

where $\mathcal{L}_{grid}$ enforces meteorological fidelity at the WRF grid scale, and $\mathcal{L}_{station}$ enforces point-level accuracy at weather stations—directly relevant for infrastructure risk. The balance parameter α was tuned empirically and set to 0.01 in this study.

C. Power Transmission System Risk Forecasting

To bridge the Risk Gap, the 500-m wind field $\widehat{\boldsymbol{Y}}_{\mathrm{ds}}$ is fed into a 4-step risk mapping process based on standard power system fragility modeling:

Step 1. Wind field interpolation: Forecasted hourly 500-m wind fields are interpolated to the precise 3D coordinates of each of the 32,458 transmission towers, yielding the tower-level wind speed $v_j(t)$ and attack angle $\theta_j(t)$ for each tower j.

Step 2. Instantaneous failure probability: The instantaneous failure probability $P'_{f,j}(t)$ for each tower is calculated using an angle-dependent lognormal fragility function Φ [14]:

$$P'_{f,j}(t) = \Phi\left[\frac{\ln\left(v_j(t)\right) - \mu_{\theta_j}}{\sigma_{\theta_j}}\right] \tag{6}$$

where μ_{θ_j} and σ_{θ_j} are the log-mean and log-standard deviation parameters associated with wind attack angle θ. Resistance uncertainty is propagated via Monte Carlo simulation (MCS) by sampling resistance parameters and evaluating the fragility model for each sample. Details on transmission tower fragility modeling can be found in [15]-[17].

Step 3. Cumulative tower risk: The cumulative failure probability $P_{f,j}(t)$ up to time t with time-invariant resistance $R = r$, is calculated using a survival update, which enforces that a failed tower remains failed:

$$P_{f,j}(t) = P_{f,j}(t-1) + \sum_{r \in R}\left(1 - P_{f,j|r}(t-1)\right) \cdot P'_{f,j|r}(t) \cdot P(R = r) \tag{7}$$

where $P'_{f,t|r}(t)$ is instantaneous probability of tower collapse at time t only under load S_t conditional on a sampled resistance realization $R = r$.

Step 4. Line-level risk aggregation: A transmission line i is modeled as a series system: the line fails if any of its n_i towers fail. Accordingly, the line failure probability $P_{line,i}(t)$ is computed as one minus the joint survival probability of its towers:

$$P_{f,t}^{line,i} = 1 - \sum_{\vec{r} \in \vec{R}} \prod_{j=1}^{n_i}\left(1 - P_{f,t|r_j}^{tower,j}\right) \cdot P\left(\vec{R} = \vec{r}\right) \tag{8}$$

where j indexes the total n_i towers supporting line i; $P_{f,t|r_j}^{tower,j}$, obtained from Equation 7, is the failure probability of tower j up to time t conditional on $R_j = r_j$; The vector $\vec{r}$ collects mutually correlated realizations for all n_i towers obtained by MCS of the resistance vector $\vec{R}$.

For illustrative purposes, we adopt two simplifications. First, we apply a uniform low-capacity fragility model to all towers, with parameters adjusted based on the literature [15]–[17], instead of deriving tower-specific models via computationally intensive finite-element analysis. Specifically, we set a constant logarithmic standard deviation σ_θ = 0.03 and vary the logarithmic mean μ_θ with attack angle: 2.708 (0°), 2.996 (30°), 3.219 (45°), 3.401 (60°), and 3.555 (90°). Second, we treat the supporting towers as statistically independent. While current modeling neglect other failure mechanisms (e.g., galloping and debris impact) and correlation effects, ACDF provides the high-resolution hazard inputs needed to drive more detailed multi-physics and correlated-reliability models when available. Moreover, the present implementation is deterministic; uncertainty could be incorporated by (i) running ACDF across AIWP ensemble members to propagate forecast spread, (ii) replacing the downscaling module with conditional generative models (e.g., diffusion model/generative adversarial network) to sample fine-scale realizations, and (iii) quantifying fragility uncertainty via finite element method-informed parameter estimation coupled with MCS.

IV. Results and Case Study

We validate the framework using a Leave-One-Storm-Out (LOSO) protocol. The results for the Typhoon Hagupit (2020) case study are presented, as this storm was withheld from training.

A. Correcting & Downscaling Pangu-Weather Forecasts

The performance of the proposed ACDF framework was first evaluated at the hazard level by comparing corrected and downscaled wind forecasts against 2,513 station observations across five LOSO test events. Results were benchmarked against the raw Pangu-Weather forecast and the HRCLDAS analysis, as summarized in Table I.

The raw Pangu-Weather forecast exhibits substantial errors, with an average MAE of 2.245 m/s and a pronounced positive bias (ME = 1.584 m/s), reflecting systematic intensity overestimation and insufficient representation of local wind variability. Introducing the correction module (ACDF-Corr.) significantly improves forecast skill: by assimilating recent observations, large-scale storm biases are effectively removed, reducing the MAE by 35.5% to 1.447 m/s.

Building on the corrected background flow, the terrain-aware downscaling stage injects high-resolution topographic structure. The full ACDF reduces the MAE to 1.374 m/s, a 38.8% reduction relative to the Pangu baseline. It also narrows the error spread, achieving the smallest MAE standard deviation among all models (1.515 m/s), which is important for reliable downstream risk decisions.

B. System-level Risk

To demonstrate the end-to-end workflow, we present a case study of Severe Typhoon Hagupit (2020). This event was selected because it was strictly withheld from the training data (part of the LOSO protocol) and caused the real-world failure of a transmission line, providing a clear ground truth for risk

TABLE I
STATION-SCALE MEAN ± STANDARD DEVIATION OF MAE AND ME FOR FIVE LOSO TEST STORMS
(BEST MEAN VALUES IN **BOLD**; SECOND-BEST IN UNDERLINE)

Testing Event (ID)	Metric	Model			
		Pangu	ACDF-Corr.	ACDF (Ours)	HRCLDAS (Target)
Haikui (1211)	MAE_{spd} (m/s)	2.374±1.890	1.600±1.696	**1.419±1.506**	1.705±1.783
	ME_{spd} (m/s)	1.821±2.427	**-0.073±2.330**	-0.168±2.062	0.190±2.459
	MAE_{dir} (°)	38.668±40.559	37.341±40.528	**36.008±39.857**	39.282±42.441
Lekima (1909)	MAE_{spd} (m/s)	2.705±2.052	1.631±1.813	**1.594±1.760**	1.600±1.811
	ME_{spd} (m/s)	1.948±2.780	-0.505±2.386	**-0.385±2.343**	-0.230±2.406
	MAE_{dir} (°)	42.266±43.585	39.906±42.535	**39.529±42.434**	39.154±42.074
Mitag (1918)	MAE_{spd} (m/s)	2.001±1.697	1.329±1.501	**1.299±1.452**	1.252±1.502
	ME_{spd} (m/s)	1.315±2.270	0.582±1.919	**-0.488±1.886**	-0.189±1.946
	MAE_{dir} (°)	47.194±44.504	43.747±43.661	**43.403±43.484**	40.321±41.913
Hagupit (2004)	MAE_{spd} (m/s)	1.792±1.604	1.296±1.418	**1.233±1.343**	1.166±1.328
	ME_{spd} (m/s)	1.128±2.124	-0.718±1.782	**-0.585±1.727**	-0.429±1.715
	MAE_{dir} (°)	43.866±42.581	42.257±42.528	**40.810±41.949**	38.822±40.656
Muifa (2212)	MAE_{spd} (m/s)	2.452±1.597	1.360±1.510	**1.309±1.431**	1.287±1.456
	ME_{spd} (m/s)	1.827±2.287	-0.604±1.940	**-0.456±1.885**	-0.394±1.903
	MAE_{dir} (°)	45.873±43.613	42.450±43.103	**41.448±42.480**	40.325±42.812
Average	MAE_{spd} (m/s)	2.245±1.820	1.447±1.604	**1.374±1.515**	1.404±1.605
	ME_{spd} (m/s)	1.584±2.418	-0.501±2.102	**-0.421±2.002**	-0.212±2.121
	MAE_{dir} (°)	43.314±43.087	40.994±42.483	**40.088±42.080**	39.476±41.899

validation. We analyze the 12-hour forecast initialized at 12:00 UTC on Aug. 3, 2020. At this cycle, ACDF ingested the past 6 hours of observations together with the Pangu forecast and generated 12-hour, 500-m hazard and risk predictions over the 105,500 km² Zhejiang grid. The full pipeline (correction, downscaling, and risk mapping) was executed in approximately 25 s, which indicates operational feasibility.

The value of ACDF is evident in the landfall-time hazard forecast (19:00 UTC, a 7-hour lead), as shown in Fig. 2(a–c). The raw Pangu forecast (Fig. 2(a)) is overly smooth and weak, failing to capture the compact, high-wind core of the typhoon near the coast. The correction-only module, ACDF-Corr. (Fig. 2(b)), restores storm intensity and improves the mesoscale structure. Finally, the full ACDF (Fig. 2(c)) preserves these storm-scale corrections and superimposes critical 500-m terrain-conditioned details.

These hazard differences translate directly to the system-level risk maps in Fig. 2(d–f). Using the raw Pangu-Weather forecast (Fig. 2(d)), the derived map shows virtually no risk across the grid because the coarse, smoothed wind field never triggers the failure thresholds. In contrast, the ACDF-driven map (Fig. 2(e)) highlights a narrow, high-risk coastal corridor that matches the recorded failures (Fig. 2(f)), including the failed Line 73. For Line 73, the predicted failure probability reached 100% at 18:00 UTC, 5 hours before the recorded failure time, providing actionable lead time. ACDF also flagged Line 68 as high risk; although it did not collapse, it experienced a forced outage due to severe galloping, which is consistent with the localized high-wind forecast. While the high collapse probability partly reflects the conservative uniform-fragility assumption, this result shows that ACDF can pinpoint vulnerable corridors that the baseline model misses.

Due to strict data security regulations, the grid topology employed in this study is location-shifted, with historical damage records mapped to the nearest transmission lines. Consequently, our validation prioritizes identifying high-risk corridors at the line level rather than establishing a precise, one-to-one correspondence for individual tower failures.

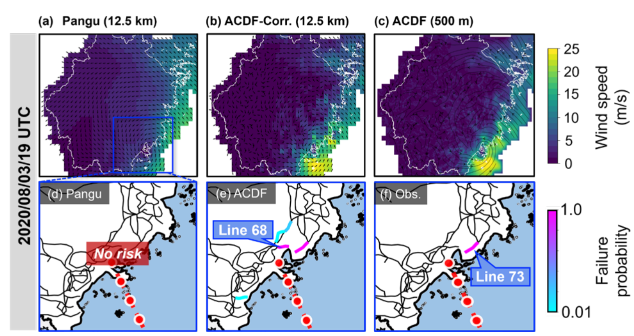

Figure 2. Comparison of (a) Pangu, (b) ACDF-Corr., and (c) ACDF wind fields at 19:00 UTC on Aug. 3, 2020; and line failure probabilities at the same time, comparing (d) Pangu and (e) ACDF against (f) recorded line failures.

C. *Asset-level Risk*

In the landfall segment with rugged relief, the correction-only run (ACDF-Corr.) leaves span loads essentially flat along Line 73, yielding uniformly low tower-failure likelihoods. Activating the full ACDF changes the picture: flow acceleration in valleys and over ridgelines is explicitly resolved, creating pockets of wind near 20 m/s and large tower-to-tower gradients in $P_{j,t}$. Fig. 3(a) renders the final tower probabilities atop local topography; Fig. 3(b) traces, along the line, the final P_j, the peak wind between 13:00–00:00 UTC, and elevation. The three curves align tightly, where higher orographic exposure coincides with wind maxima and concentrated failure hotspots. These fine-scale signals make the results operationally actionable, identifying the specific spans and towers to prioritize for pre-emptive switching, targeted inspection, and phased restoration.

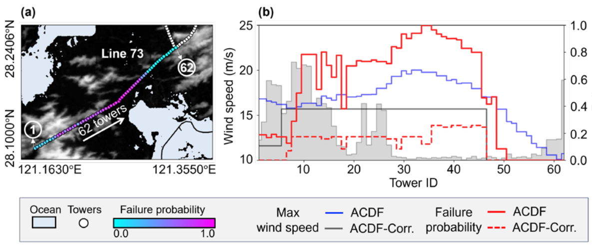

Figure 3. (a) Surrounding topography and final failure probabilities of Line 73; (b) final failure probabilities, maximum wind speeds from 13:00 UTC on Aug. 3, 2020, to 00:00 UTC on Aug. 4, 2020, and tower elevations along Line 73.

V. Conclusion

This paper proposes an AI-driven framework (ACDF) to bridge the gap between coarse AIWP and operational power grid resilience. By integrating a two-stage correction-downscaling model with fragility mapping, ACDF translates global forecasts into real-time, asset-level failure probabilities. Validated across five storms, the framework reduced wind speed MAE by 38.8% (to 1.374 m/s) compared to raw Pangu-Weather, significantly enhancing reliability. In the Typhoon Hagupit (2020) case study, ACDF successfully predicted a real-world line failure with a 5-hour lead time, an event missed by the baseline model, while generating 500-m province-wide risk maps in approximately 25 seconds, demonstrating operational feasibility for fast decision support.

Although the present analysis focused on a single forecast member, the framework is ensemble-ready: driven by compact AIWP ensembles, ACDF can yield multi-scenario hazard and risk maps that bracket the most-likely evolution and stress-test adverse yet plausible outcomes, providing actionable uncertainty bands for crew pre-positioning, network reconfiguration, and staged restoration. Looking ahead, future work will focus on three key directions. First, since the current framework is trained and validated in Zhejiang, we aim to incorporate broader datasets to verify its applicability in other typhoon-prone regions. Second, we plan to expand the event set to capture diverse storm characteristics, such as rapid intensification cycles, and extend the pipeline to multi-hazard settings (e.g., flood, ice and snow) for comprehensive resilience. Finally, assessing the model's generalization across different grid topologies by integrating refined, physics-based fragility models remains a priority for further research.

Acknowledgment

This research was co-supported by Zhejiang Department of Science & Technology (Grant No. 2024C03255) and by the State Grid Zhejiang Electric Power Co., Ltd. (Grant No. 5211DS25000L).

References

[1] World Meteorological Organization (2021), WMO Atlas of Mortality and Economic Losses from Weather, Climate and Water Extremes (1970–2019) [Online]. Available: https://library.wmo.int/idurl/4/57564

[2] J. L. Beven II, R. Berg, and A. Hagen, "Tropical Cyclone Report: Hurricane Michael (AL142018)," National Hurricane Center, Miami, FL, USA, May 2019. [Online]. Available: https://www.nhc.noaa.gov/data/tcr/AL142018_Michael.pdf

[3] U.S. Department of Energy, Infrastructure Security & Energy Restoration, "Tropical Cyclone Michael | Report #13," U.S. Dept. of Energy, Washington, D.C., USA, Situation Rep., Oct. 16, 2018. [Online]. Available: https://www.energy.gov/sites/default/files/2018/10/f56/Michael%20DOE%20Event%20Summary%20Report%20%2313%20Morning%20October%2016%2C%202018.pdf

[4] K. Bi, L. Xie, H. Zhang, X. Chen, X. Gu, and Q. Tian, "Accurate medium-range global weather forecasting with 3D neural networks," Nature, vol. 619, no. 7970, pp. 533–538, 2023.

[5] R. Lam, A. Sanchez-Gonzalez, M. Willson, et al., "Learning skillful medium-range global weather forecasting," Science, vol. 382, no. 6676, pp. 1416–1421, 2023.

[6] X. Huang and N. Wang, "An adaptive nested dynamic downscaling strategy of wind-field for real-time risk forecast of power transmission systems during tropical cyclones," Reliability Engineering & System Safety, vol. 242, Art. no. 109731, 2024.

[7] M. Reichstein, V. Benson, J. Blunk, et al., "Early warning of complex climate risk with integrated artificial intelligence," Nature Communications, vol. 16, no. 1, Art. no. 2564, 2025.

[8] Y. Wu, N. Wang, X. Huang, and Z. Wang, "Enhancing power grid resilience during tropical cyclones: Deep learning-based real-time wind forecast corrections for dynamic risk prediction," Reliability Engineering & System Safety., vol. 263, Art. no. 111284, 2025.

[9] B. Wu, W. Chen, W. Wang, B. Peng, L. Sun, & L. Chen, "WeatherGNN: Exploiting Meteo- and Spatial-Dependencies for Local Numerical Weather Prediction Bias-Correction," arXiv preprint arXiv:2310.05517, 2024.

[10] M. Mardani, N. Brenowitz, Y. Cohen, J. Pathak, C.Y. Chen, C.C. Liu, A. Vahdat, M.A. Nabian, T. Ge, A. Subramaniam, K. Kashinath, J. Kautz, & M. Pritchard, "Residual corrective diffusion modeling for km-scale atmospheric downscaling," Communications Earth & Environment, vol. 6, Art. no. 124, 2025.

[11] S. Han, B. Liu, C. Shi, Y. Liu, M. Qiu, and S. Sun, "Evaluation of CLDAS and GLDAS Datasets for Near-Surface Air Temperature over Major Land Areas of China," Sustainability, vol. 12, no. 10, Art. no. 4311, 2020.

[12] Z. Wu, S. Pan, G. Long, J. Jiang, X. Chang, and C. Zhang, "Connecting the Dots: Multivariate Time Series Forecasting with Graph Neural Networks," in Proc. 26th ACM SIGKDD International Conf. on Knowledge Discovery & Data Mining, Virtual Event, CA, USA, 2020, pp. 753–763.

[13] Z. Wang, X. Cun, J. Bao, W. Zhou, J. Liu, and H. Li, "Uformer: A General U-Shaped Transformer for Image Restoration," in Proc. 2022 IEEE/CVF Conf. on Computer Vision and Pattern Recognition (CVPR), New Orleans, LA, USA, pp. 17662–17672.

[14] JCSS (Joint Committee on Structural Safety), Probabilistic Model Code. Part 3: Resist. Models, 2001.

[15] X. Fu, H.N. Li, L. Tian, J. Wang and H. Cheng, "Fragility analysis of transmission line subjected to wind loading," Journal of Performance of Constructed Facilities, vol. 33, no. 4, 2019.

[16] Y. Cai, Q. Xie, S. Xue, L. Hu and A. Kareem, "Fragility modelling framework for transmission line towers under winds," Engineering Structures, vol 191, pp. 686-697, 2019.

[17] J. Xue, F. Mohammadi, X. Li, M. Sahraei-Ardakani, G. Ou, and Z. Pu, "Impact of transmission tower-line interaction to the bulk power system during hurricane," Reliability Engineering & System Safety, vol. 203, Art. no. 107079, 2020.

979-8-3315-8138-1